(Received 7 May 2026, Accepted 9 June 2026, Scheduled 20 June 2026)

High Gain Narrow Beam SIW Antenna for MillimeterWave Radar and Emerging Portable Wireless Applications

Umasankar P. Ananthasankar[1,*], Thulaseedharan K. Rekha[1], and Anju P. Mathews[2]

[1] *NSS College, Rajakumari, Affiliated to Mahatma Gandhi University, Kottayam, Kerala, India*
[2] *St. Joseph's College Moolamattom, Idukki, Kerala, India*

ABSTRACT: This paper presents a high-gain substrate-integrated waveguide antenna featuring a narrowly-focused radiation beam with enhanced cross-polarization characteristics, specially designed for precision millimeter-wave radar systems and n-257 band point-to-point 5G wireless applications. The antenna incorporates a novel design with dual radiator slots arranged both vertically and horizontally on the broadside wall of the substrate-integrated waveguide, forming a Non-Intersecting Asymmetrical T-shaped unit cell. This unit cell is periodically distributed to create an eight-element radiator array, thereby improving the antenna's gain and bandwidth. The antenna operates in the frequency range from 27 GHz to 28.54 GHz, thereby covering the n-257 5G frequency band. Moreover, it exhibits a half-power beamwidth of 8.1°, low side-lobe level of −13.3 dB, and cross-polarization discrimination level of 25 dB, making it suitable for high-precision millimeter-wave radar sensing applications. The proposed design provides a peak gain of 10.51 dBi with a radiation efficiency of 84.82%. Moreover, the integration of a dome-shaped polytetrafluoroethylene dielectric lens achieves a peak gain of 12.50 dBi with an enhanced radiation efficiency of 86.35%. The antenna design and simulation were performed using CST Studio Suite, followed by an experimental validation. Owing to its high gain, low side-lobe levels, and a sharply focused main-lobe beam with excellent cross-polarization discrimination, the antenna is well-suited for millimeter-wave radar sensing and point-to-point 5G communication systems.

1. INTRODUCTION

The advancements in telecommunication and information technology have significantly increased the demand for portable wireless devices, intelligent personal assistants, Internet of Things (IoT) systems, and AI-enabled smart platforms [1]. Frequency bands below 10 GHz are widely utilized for wireless technologies, such as mobile communication, Wi-Fi, Bluetooth, and industrial, scientific, and medical (ISM) applications. However, the limited spectrum available in these bands, combined with rapidly increasing demand for wireless data traffic, results in spectrum congestion and increased interference, degrading the network performance and communication reliability [2]. To meet the growing requirements for bandwidth and channel capacity in modern communication systems, migration from conventional lower microwave frequency bands to higher frequency bands has become essential. This transition can provide improved data throughput, greater channel capacity, reduced latency, and fewer network interruptions and dropouts, thereby ensuring reliable and consistent wireless services [3, 4]. The millimeter-wave (mm-Wave) frequency bands are particularly attractive for portable wireless devices because of their ability to provide higher gain and wider bandwidth with compact antenna structures. In addition, mm-Wave frequencies are highly suitable for radar applications because they offer a higher spatial resolution and narrower half-power beamwidth (HPBW), enabling more accurate detection and imaging [5]. Despite these benefits, mm-Wave signals are highly susceptible to propagation losses and atmospheric attenuation, especially rain fade, which may affect communication reliability [6]. In [7], an orthogonal asymmetrical slot-based λ-shaped radiating element substrate integrated waveguide (SIW) antenna is presented. This configuration provides dual-band operation at 10.76 GHz and 12.39 GHz with a radiation efficiency of 82.5%. However, the antenna exhibits a very narrow impedance bandwidth of less than 3.5% in both operating bands. A planar SIW antenna with a T-shaped cross-slot configuration is presented in [8]. The antenna operates over the 8.8 GHz to 10.9 GHz frequency range, achieving a peak gain of 7.3 dBi with a radiation efficiency of 84.7%. The design's limitation is relatively high back-lobe radiation. In [9], an L-shaped SIW cavity-backed antenna array for X-band applications is reported. The antenna operates over the frequency range of 9.4 GHz to 10.5 GHz with a peak gain of 9.5 dBi. However, the radiation pattern is not highly directional. A wideband 1×4 SIW patch dipole array antenna is presented in [10]. The antenna achieves a wide impedance bandwidth ranging from 24.12 GHz to 30.83 GHz with a peak gain of 11.02 dBi. Despite these benefits, the antenna structure is relatively complex due to the requirement of an additional intermediate slot-coupling layer. In [11], a complementary split-ring resonator (CSRR) based filtering SIW antenna is presented. The design provides dual-band operation at 10.2 GHz and 16.9 GHz, with a peak gain exceeding 11 dBi in both frequency bands. A key advantage of this antenna is the good isolation between the two op-

* Corresponding author: Umasankar Prasad Ananthasankar (electrotechnet@gmail.com).

erating bands, achieved through the incorporation of the CSRR filtering structure. A cavity-backed metamaterial-based SIW antenna operating at 27.42 GHz and 28.70 GHz is presented in [12]. The primary drawback of the design is its limited performance, with a gain of only 4.7 dBi and a bandwidth of 300 MHz at 28.70 GHz. A highly directive eight-element SIW array antenna operating at 28 GHz with a gain of 13 dBi is reported in [13]. Despite its high directivity, the antenna has a limited bandwidth of 550 MHz, limiting its applicability in broadband systems. A cavity-backed triangular-ring-slot SIW antenna presented in [14] uses a central slot to form a twin-ring structure operating at 14.5 GHz and has a bandwidth of 2.09 GHz. However, the gain remains below 5 dBi. A wide-band cavity-backed SIW L-shaped slot antenna operates over 25.1 GHz to 29 GHz with a 14.4% bandwidth and a peak gain of 7.5 dBi is reported [15]. A compact mushroom-shaped SIW patch antenna with an impedance bandwidth of 25.98 GHz to 40.18 GHz and a gain of 7.2 dBi is presented in [16]. Despite achieving relatively high gain and wide bandwidth, these antennas exhibit a broader HPBW, which limits their suitability for high-precision mm-Wave radar imaging applications.

This paper introduces a compact high-gain SIW antenna operating in 27 GHz to 28.54 GHz frequency range, dedicated to mm-Wave radar sensors and point-to-point 5G wireless communications. The proposed antenna employs a novel dual-slot radiator configuration, with vertically and horizontally oriented slots on the broadside wall of the SIW to form a Non-Intersecting Asymmetrical-T (NIAT) shaped unit cell. These unit cells are arranged between the rows of conductive vias and are periodically repeated to form an eight-element radiator array, significantly improving the bandwidth and gain of the antenna. The antenna achieved a bandwidth of 1.54 GHz, a peak gain of 10.51 dBi, and a radiation efficiency of 84.82%. In addition, a polytetrafluoroethylene (PTFE)-based dielectric lens antenna (DLA) arrangement further enhances the gain up to 12.50 dBi with an efficiency of 86.35%. The proposed antenna offers high gain, a focused narrow beam, low side-lobe levels, and high cross-polarization discrimination (XPD). These features ensure efficient beam radiation and reduced interference, making it a suitable choice for mm-Wave radar sensing and emerging point-to-point high-speed wireless communication systems.

2. ANTENNA GEOMETRY AND DESIGN

The antenna structure is realized on an SIW platform. It combines the low-loss and high-power-handling capabilities of metallic waveguides with the compactness of planar printed circuit board technology [17]. A Rogers RT/Duroid 5880 substrate with a thickness of 0.50 mm and relative permittivity of 2.2 serves as the substrate for the proposed antenna. A copper broadside section with a length of 67.50 mm and a width of 5.50 mm is used to accommodate the radiating elements. Eight NIAT unit cells are periodically distributed along the broadside wall of the SIW structure to realize an array configuration, as illustrated in Figure 1. The structural parameters are presented in Table 1.

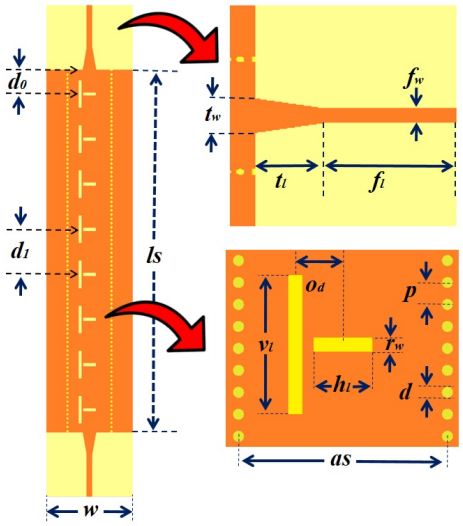

FIGURE 1. Antenna structure.

2.1. Design of via Interconnection

The SIW structure is formed by top and bottom conductive layers separated by a low-loss dielectric substrate, interconnected by two parallel rows of metallized via configuration as shown in Figure 2. These vias act as radio frequency (RF) shielding walls, effectively confining electromagnetic energy and suppressing radiation leakage outside the structure [18]. The group of conducive vias emulates the sidewalls of a conventional rectangular waveguide, thereby enabling electromagnetic wave propagation.

To ensure proper electromagnetic confinement and minimize radiation leakage, the dimensions of conductive vias are precisely calculated in accordance with established design guidelines [19, 20]. In order to keep radiation loss minimal, the dimension of via diameter "d" and pitch distance "p" should satisfy the condition specified in Eq. (1).

$$d < \frac{\lambda g}{5} \quad \text{and} \quad p < 2d \tag{1}$$

where λg is the guided wavelength. Based on Eq. (1), the calculated value of via diameter "d" is 0.3 mm, and pitch distance "p" is 0.6 mm to ensure proper wave confinement within the intended operating frequency band. The effective width "as" determines the passband characteristics of the SIW structure, which is analogous to the width of a conventional metallic rectangular waveguide. It determines the cut-off frequency and propagation characteristics of the dominant mode. The effective width can be calculated using Eqs. (2)–(5). In a rectangular waveguide, the cut-off frequency, "fc", can be obtained from Eq. (2)

$$fc = \frac{c}{2\pi}\sqrt{\left(\frac{m\pi}{a}\right)^2 + \left(\frac{n\pi}{b}\right)^2} \tag{2}$$

where "c" is the speed of light; "m and n" represent the number of modes; "a and b" are the dimensions of the waveguide. For dominant mode transmission, the dimension "b" can be omitted.

TABLE 1. Antenna dimensions.

Parameter	Dimension (mm)	Description
d_0	4.20	Distance of NIAT cell from taper transition
d_1	8.40	Distance between adjacent NIAT cell
h_l	1.77	Horizontal radiator length
v_l	4.85	Vertical radiator length
r_w	0.4	Radiator width
o_d	1.3	Offset distance
p	0.6	Pitch distance
d	0.3	Diameter of the via
f_w	0.8	Feed width
f_l	6.0	Feed length
t_l	3.12	Taper length
t_w	2.0	Taper width
ls	67.50	Length
as	5.50	Effective width

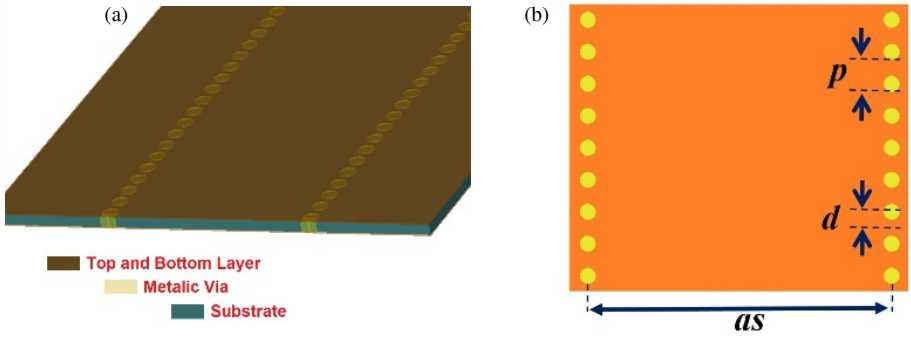

FIGURE 2. SIW structure, (a) cross-sectional view, (b) broadside wall view.

Then Eq. (2) becomes

$$fc = \frac{c}{2a} \tag{3}$$

In the case of dielectric-filled waveguide structures, such as SIW, Eq. (3) becomes

$$fc = \frac{c}{2a\sqrt{\varepsilon_r}} \tag{4}$$

where "ε_r" is the relative permittivity of the substrate material. The effective width "*as*" is determined by

$$as = w - \frac{d^2}{0.95p} \tag{5}$$

where "w" is the width of the substrate. Based on Eq. (5), the effective width "*as*" was found to be 5.45 mm and optimized to 5.50 mm for the desired operating frequency band.

2.2. Design of Radiator Slot

A radiator slot in an SIW structure is formed by etching a portion of the metallic broadside wall surface, forming an aperture area with a specific length and width. When the SIW is excited by RF energy, the electromagnetic fields propagate along with the SIW structure. The presence of the slot introduces a discontinuity in the current distribution on the conducting surface, allowing a portion of the confined energy to radiate into free space. The antenna dimensions were computed using Eqs. (6)–(7). The guided wavelength (λg) inside a rectangular air-filled waveguide can be obtained by

$$\lambda g = \frac{\lambda o}{\sqrt{1 - \left(\frac{\lambda o}{\lambda c}\right)^2}} \tag{6}$$

where λo and λc are the free space wavelength and cut-off wavelength, respectively. For a dielectric-filled medium, such as SIW, the relative permittivity "ε_r" is considered, and then Eq. (6) becomes,

$$\lambda g = \frac{\lambda o}{\sqrt{\varepsilon_r - \left(\frac{\lambda o}{\lambda c}\right)^2}} \tag{7}$$

Each slot is designed to resonate at a specific frequency, with its length typically chosen close to half the guided wavelength.

In practice, fractions of the free space wavelength, such as $\lambda_o/4$ or $\lambda_o/8$, may also be used for miniaturization [21]. To achieve in-phase radiation, the first slot is placed at a distance of $\lambda g/4$ from the excitation source. The subsequent slots are spaced $\lambda g/2$ apart, so that the fields radiated from each slot add the electromagnetic waves constructively in the far field. This configuration provides high gain and directivity at a single frequency. Here, an asymmetrical slot configuration is employed to achieve a boarder bandwidth and gain. The vertical slot length "v_l" is optimized to 4.85 mm, corresponding to $\lambda_o/2$ of the lower 27 GHz band, while the horizontal slot length "h_l" is optimized to 1.77 mm, corresponding to $\lambda_o/4$ of the higher 28 GHz band. The higher-frequency slot dimension is chosen as $\lambda_o/4$ to avoid physical intersection between the two slots. To achieve enhanced impedance bandwidth and gain, a novel NIAT unit cell is incorporated into the proposed design. The longer vertical slots excite the lower-frequency resonant mode due to its longer effective current path length, whereas the shorter horizontal slots are responsible for generating the higher-frequency resonance. When these two slot configurations are combined within a single unit cell, their respective resonances effectively couple and merge, resulting in a significantly broadened impedance bandwidth. Furthermore, the horizontal and vertical slots are intentionally separated by a finite offset distance to avoid direct physical interconnection. This novel design approach avoids unnecessary enlargement of the overall structure and minimizes potential degradation in impedance matching and radiation performance. A detailed breakdown simulation analysis has been carried out using a single NIAT unit cell to validate the bandwidth and gain enhancement. The simulation has been carried out by placing the radiator element at a distance of "d_0" (4.20 mm) symmetrically from both taper transition ends. The vertical slot configuration exhibits a distinct resonance around 27.60 GHz, while the horizontal slot configuration produces a resonance near 28.40 GHz. However, the NIAT unit cell exhibits a wider impedance bandwidth of 1.8 GHz spanning from 27.2 GHz to 29 GHz due to the merging and superposition of these resonant modes, as indicated by the solid curve in Figure 3(a). The gain characteristics shown in Figure 3(b) indicate that the individual horizontal and vertical slot configurations contribute only marginally to the overall gain, due to their limited effective aperture and radiation efficiency. However, when combined, a noticeable improvement is achieved. The NIAT unit-cell antenna exhibits a simulated gain of approximately 1.5 dBi at 28.2 GHz, which increases to 2.2 dBi at 29 GHz. Despite this improvement, the gain level remains relatively lower, indicating the need for further improvement. To address this, an array configuration is employed. The S_{11} results presented in Figure 3(c) demonstrate that the horizontal slot array achieves a relatively wider bandwidth at higher frequencies. Conversely, the vertical slot antenna array exhibits greater suppression at lower frequencies. Notably, the combined NIAT array configuration combines the advantages of both slot types, resulting in an enhanced impedance bandwidth of 1.9 GHz ranging from 27.1 GHz to 29 GHz. The gain enhancement achieved through array formation is further illustrated in Figure 3(d). The array consisting of only horizontal slots achieves a peak gain of approximately 7.9 dBi, and the vertical slot array reaches around 10 dBi. In comparison, the proposed novel NIAT array configuration delivers a peak gain of 11.60 dBi. This improvement is attributed to constructive interference and more efficient beam formation, leading to increased gain, as indicated by the solid curve.

The surface current distributions of the NIAT slot at 27 GHz, 28.2 GHz, and 29 GHz are illustrated in Figures 4(a)–(c), respectively. At 27 GHz, the maximum surface current density is concentrated at the ends of the longer vertical slot, indicating that the vertical slot primarily contributes to the lower resonant mode. The shorter horizontal slot exhibits weak current concentration, indicating a negligible contribution at the lower frequency band. At 29 GHz, strong current concentration is observed around the shorter horizontal slot, confirming its role in exciting the higher-order resonant mode. At 28.2 GHz, significant current distribution is observed simultaneously around both slots, indicating concurrent excitation of the two resonant structures and resulting in resonance merging and an enhanced impedance bandwidth.

.

2.3. Design of SIW to Microstrip Transition

To achieve proper impedance matching, a tapered matching section is introduced between the SMA connector and the main antenna structure, as shown in Figure 5(a), and its effect on impedance bandwidth is shown in Figure 5(b). The effective permittivity (ε_e) of the substrate can be obtained from Eq. (8).

$$\varepsilon_e = \frac{\varepsilon_r + 1}{2} + \frac{\varepsilon_r - 1}{2} \frac{1}{\sqrt{1 + 12(\frac{h}{tw})}} \tag{8}$$

where "ε_r" is the relative permittivity of the substrate, "h" the substrate height, and "tw" the width of the transition. The characteristic impedance Z_o of SIW-to-Microstrip Transition (SMT) can be obtained using Eq. (9).

$$Z_o = \sqrt{\frac{\mu_0}{\varepsilon_0 \varepsilon_r} \frac{h}{tw}} \tag{9}$$

If the tw/h ratio of the SIW structure is ≤ 1, Eq. (9) becomes,

$$Z_o = \frac{60}{\sqrt{\varepsilon o}} \ln \frac{8h}{tw} + 0.245 \frac{tw}{h} \tag{10}$$

If the tw/h ratio of the SIW structure is > 1, Eq. (9) becomes,

$$Z_o = \frac{120\pi}{\sqrt{\varepsilon o \frac{tw}{h} + 1.393 + 0.667 \ln\left(\frac{tw}{h} + 1.444\right)}} \tag{11}$$

Here, the tw/h ratio of the SIW structure is ≤ 1, and Eq. (10) is used to determine the value of "tw" as given in Eq. (12).

$$tw = h \frac{8e^x}{e^{2x} - 2} \tag{12}$$

where "x" is substituted from Eq. (13)

$$x = \left(\frac{Z_0}{60} \sqrt{\frac{\varepsilon_r + 1}{2}}\right) + \left(\frac{\varepsilon_r - 1}{\varepsilon_r + 1} \left(0.23 + \frac{0.11}{\varepsilon_r}\right)\right) \tag{13}$$

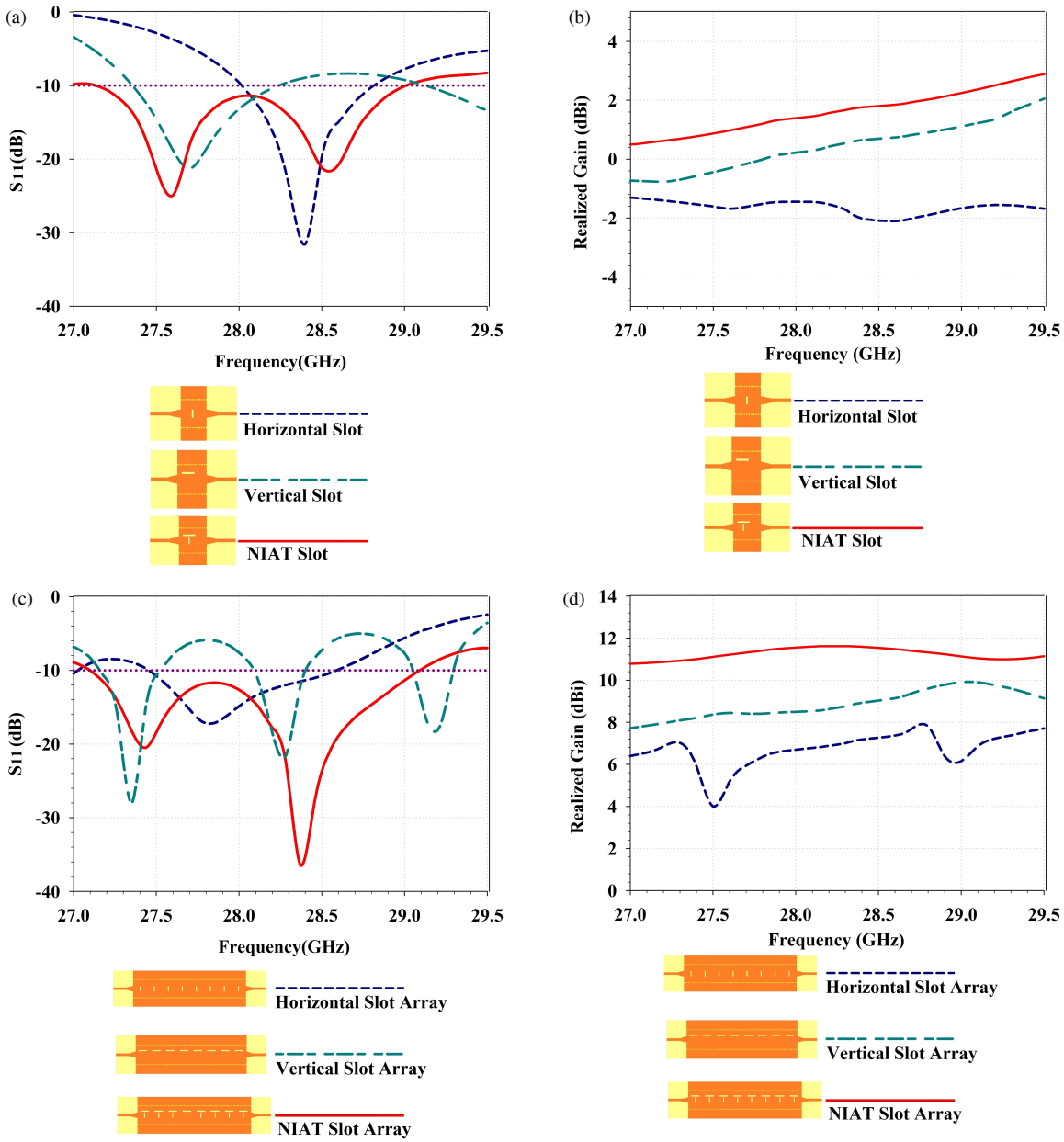

FIGURE 3. Breakdown analysis of NIAT configuration, (a) S_{11} parameters — single unit, (b) gain — single unit, (c) S_{11} parameters — array, and (d) gain — array.

The width of the feedline "fw" can be computed by Eqs. (14)–(15).

$$\frac{as}{fw} = 4.38e^{-0.627\frac{\varepsilon_r}{\varepsilon_o}} \tag{14}$$

$$fw = \frac{as}{4.38}e^{0.627\frac{\varepsilon_r}{\varepsilon_o}} \tag{15}$$

Eqs. (8)–(15) are used for SMT design [22, 23]. The taper width "tw" and feed width "fw" were initially calculated and optimized to 2.0 mm and 0.8 mm, respectively, to achieve better impedance matching.

3. PARAMETRIC OPTIMIZATION

The key design parameters of the proposed antenna were systematically varied over specific ranges to achieve optimal performance in terms of impedance matching and bandwidth. The effective width "a_s" plays a crucial role in determining the operating frequency band of the antenna. When $a_s = 4.5$ mm, the antenna fails to cover the lower-frequency region due to an increased shift in the cut-off frequency, which restricts proper wave propagation. However, increasing the effective width to 6.5 mm results in an impedance mismatch at higher frequencies. An optimal value of "a_s" is found to be 5.5 mm, which enables wideband operation over the frequency range of 27 GHz to 28.68 GHz, as illustrated in Figure 6(a). The

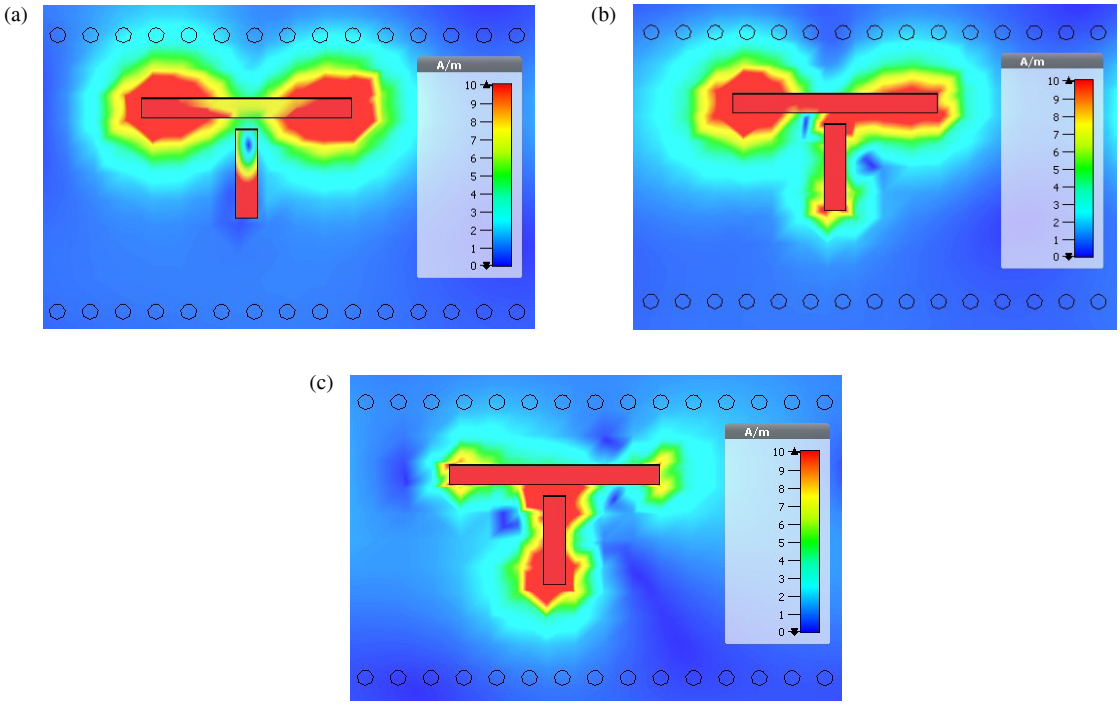

FIGURE 4. Surface current distribution (a) at 27 GHz (b) at 28.2 GHz (c) at 29 GHz.

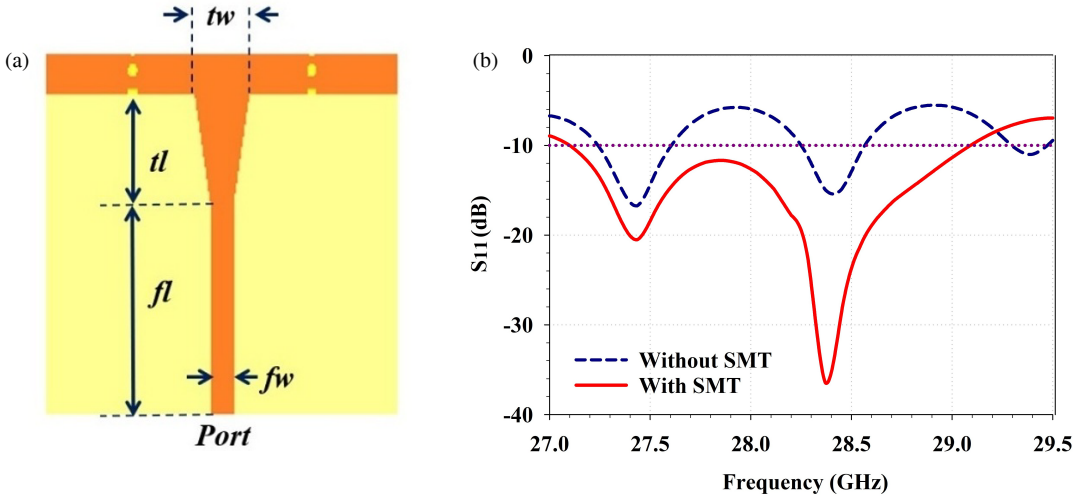

FIGURE 5. SIW to microstip transition section. (a) Broadside view and (b) S_{11} characteristics.

spacing between the intermediate NIAT elements, represented as "d_1", significantly affects both the resonant frequency and the impedance bandwidth of the antenna. A closer spacing of $d_1 = 6.2$ mm shifts the resonance toward lower frequencies due to stronger electromagnetic coupling between adjacent elements, effectively increasing the electrical length. Conversely, increasing the spacing to 10.40 mm weakens the coupling, shifting the resonance to higher frequencies. An optimized spacing of $d_1 = 8.4$ mm is found to provide the desired operating bandwidth, as shown in Figure 6(b). Furthermore, the vertical slot length, denoted as "v_l", is a key parameter in controlling the resonance behavior. It is optimized to 4.85 mm to achieve a resonant peak around the desired frequency band, as shown in Figure 6(c).

4. RADIATION PATTERN

The radiation characteristics of the antenna are analyzed in both the E-plane (Y-Z axis) and H-plane (X-Z axis) at 27.5 GHz, 28.2 GHz, and 28.5 GHz, as illustrated in Figure 7. The results demonstrate stable radiation characteristics across the 27.5 GHz to 28.5 GHz frequency range in both the E-plane and H-plane. At the resonant frequency of 28.2 GHz, the E-plane radiation pattern exhibits a highly directive beam with the maximum simulated gain of 11.60 dBi, while the measured gain is 10.51 dBi.

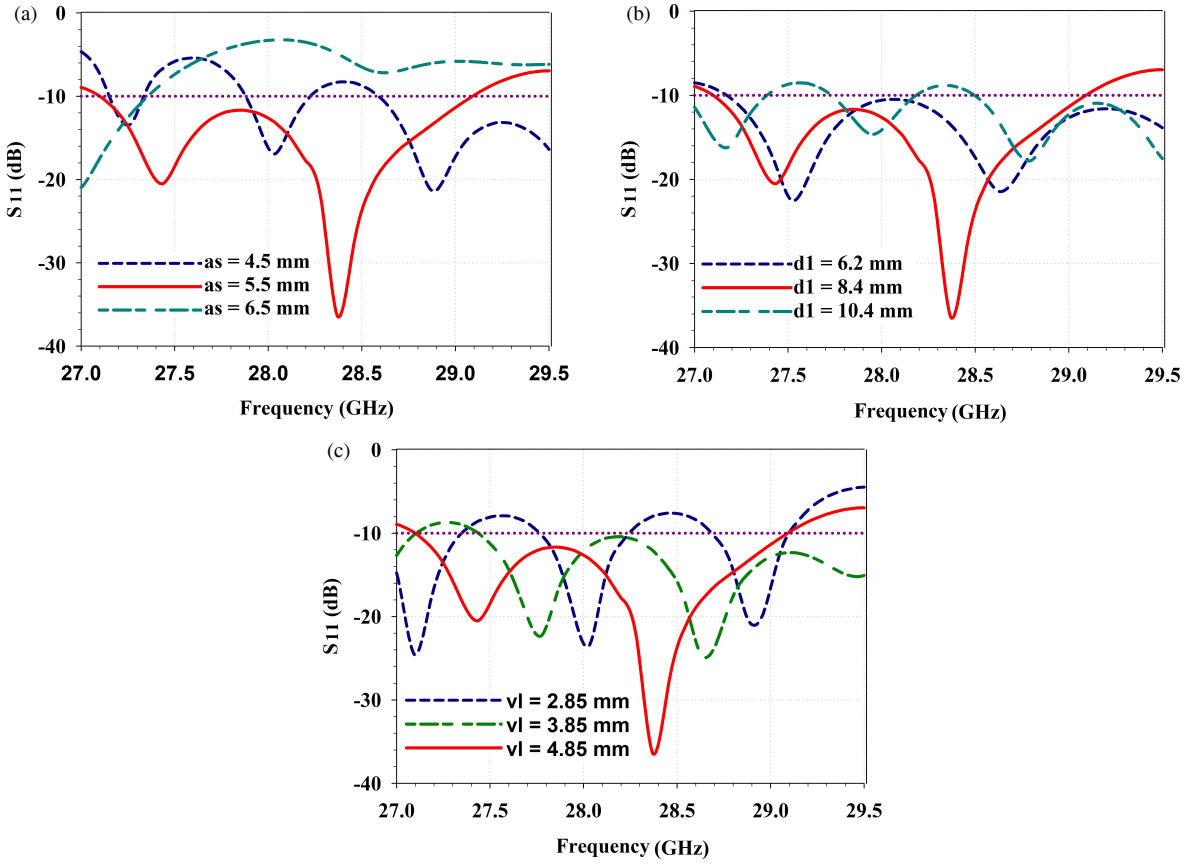

FIGURE 6. Parametric variation of S_{11} under changes in (a) effective width "as", (b) distance between radiator element "d_1", and (c) vertical slot length "v_l".

The antenna achieves a narrow HPBW of 8.1°, indicating a well-focused radiation beam along the intended direction of propagation. The side-lobe level in the E-plane is observed to be -13.3 dB, which confirms effective suppression of undesired radiation components. Furthermore, the antenna demonstrates a higher XPD level of 25 dB, ensuring good polarization purity and minimal orthogonally radiated field components. The 3D radiation patterns of the proposed antenna at the resonant frequency of 28.2 GHz in both E-plane (Y-Z axis) and H-plane (X-Z axis) are illustrated in Figure 8(a) and Figure 8(b), respectively. The results confirm that the E-plane radiation pattern is highly directive, characterized by a narrower HPBW, and the presence of side lobes is very low. As a result, the antenna concentrates energy more efficiently in a specific direction within this plane, thereby increasing directivity. In the H-plane, the radiation pattern is relatively broad and smooth, forming a dome-shaped main lobe. The electric field distribution of the proposed antenna at the resonant frequency of 28.2 GHz is illustrated in Figure 8(c). It indicates that the electric field is uniformly distributed along the radiator slot, forming constructive wave patterns due to the resonance within the structure. This uniformity indicates that the antenna efficiently supports the desired mode of operation at the desired operating frequency. A noticeable concentration of the electric field near both feed lines highlights effective coupling and efficient power transfer from the source to the radiating element. This high field intensity at the feed region confirms that minimal power is reflected back during excitation, thereby improving radiation efficiency. Furthermore, the field distribution is symmetrical about the central axis of the antenna, ensuring a stable radiation behavior and balanced operation.

5. DIELECTRIC LENS ANTENNA SETUP

A cylindrical dome-shaped PTFE-based dielectric lens with a relative permittivity of 2.1 is positioned above the radiator slots to enhance the gain of the proposed antenna. The lens focuses the radiated electromagnetic waves in the desired direction of propagation, thereby improving radiation efficiency and reducing beam spreading. The dome-shaped DLA is designed with a diameter "dm" of 7 mm and a height "dh" of 7.6 mm and fabricated with 3D printing. These dimensions are carefully optimized and positioned above the radiating aperture to optimize the field collimation, resulting in improved gain. The radiated waves from the slot antenna enter the dielectric medium, where its phase velocity decreases, causing the wave fronts to bend and converge. Owing to the dome-shaped geometry, different portions of the wave experience controlled phase delays, effectively transforming the spherical wave front emitted by the slot into a more planar wave front at the lens aperture. This phase correction mechanism reduces beam divergence and enhances radiation in the boresight direction, resulting in improved an-

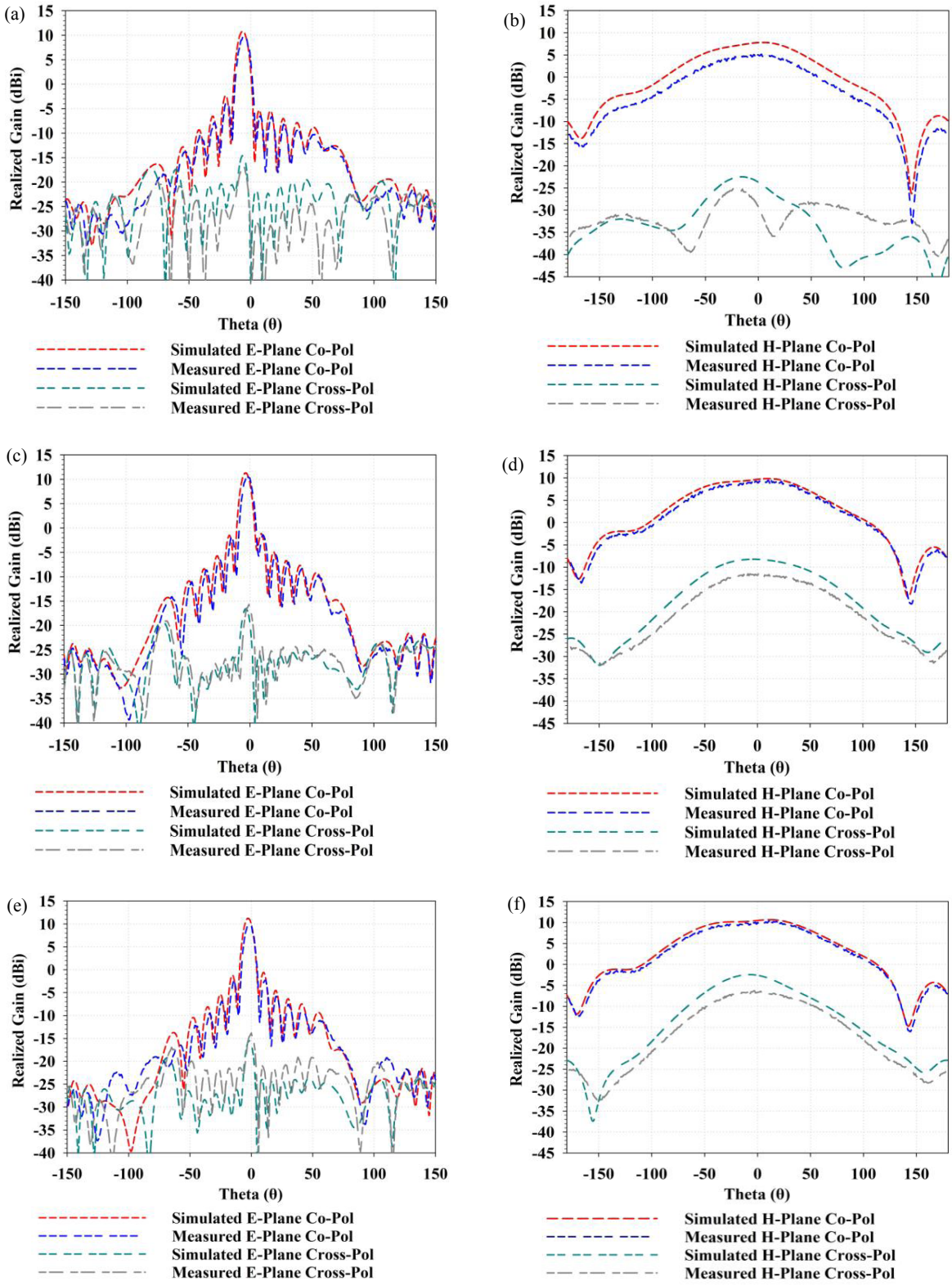

FIGURE 7. Radiation pattern at both E-plane (Y-Z axis) and H-plane (X-Z axis) at 27.5 GHz (a) & (b), 28.2 GHz (c) & (d), 28.5 GHz (e) & (f).

tenna gain. The simulated model of the dielectric lens system is shown in Figure 9(a). The fabricated prototype is presented in Figure 9(b). The measured gain and efficiency matrices are shown in Figure 9(c) and Figure 9(d), respectively. The results indicate that the measured gain increases from 10.51 dBi to 12.50 dBi, and the radiation efficiency improves from 84.82% to 86.35% with the addition of the DLA. These results confirm that the incorporation of the DLA improves both the gain and radiation efficiency.

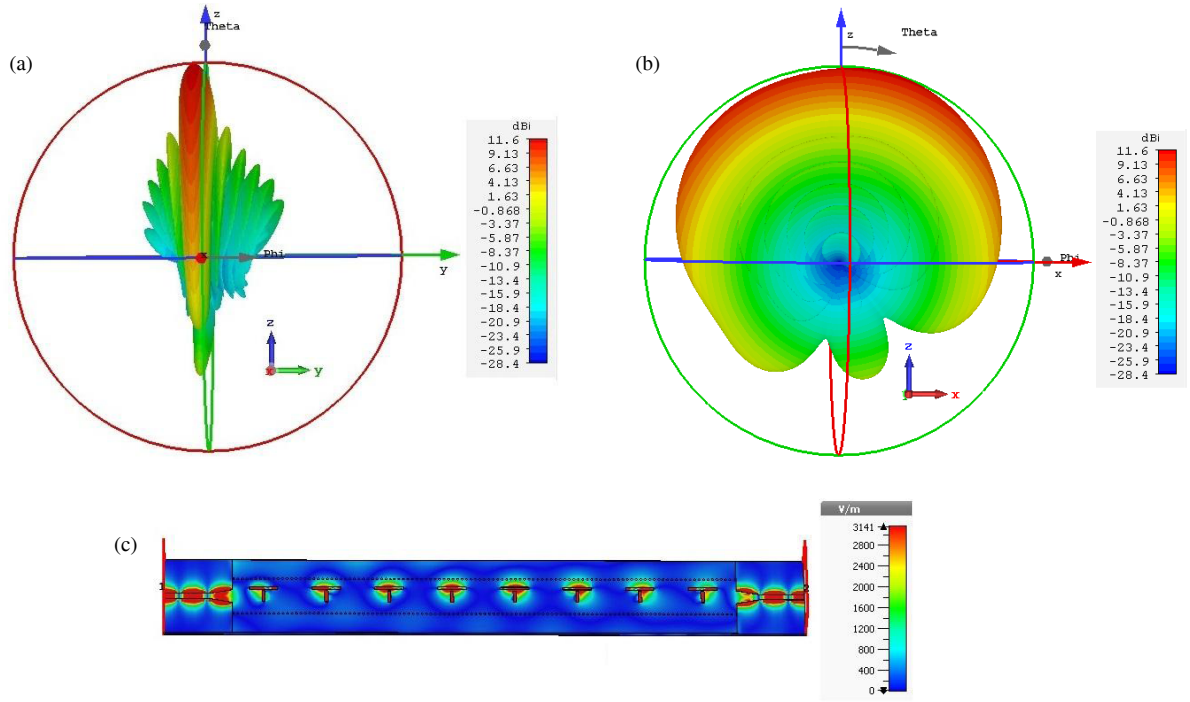

FIGURE 8. The 3D radiation pattern, (a) E-plane (Y-Z axis), (b) H-plane (X-Z axis), and (c) electric field distribution.

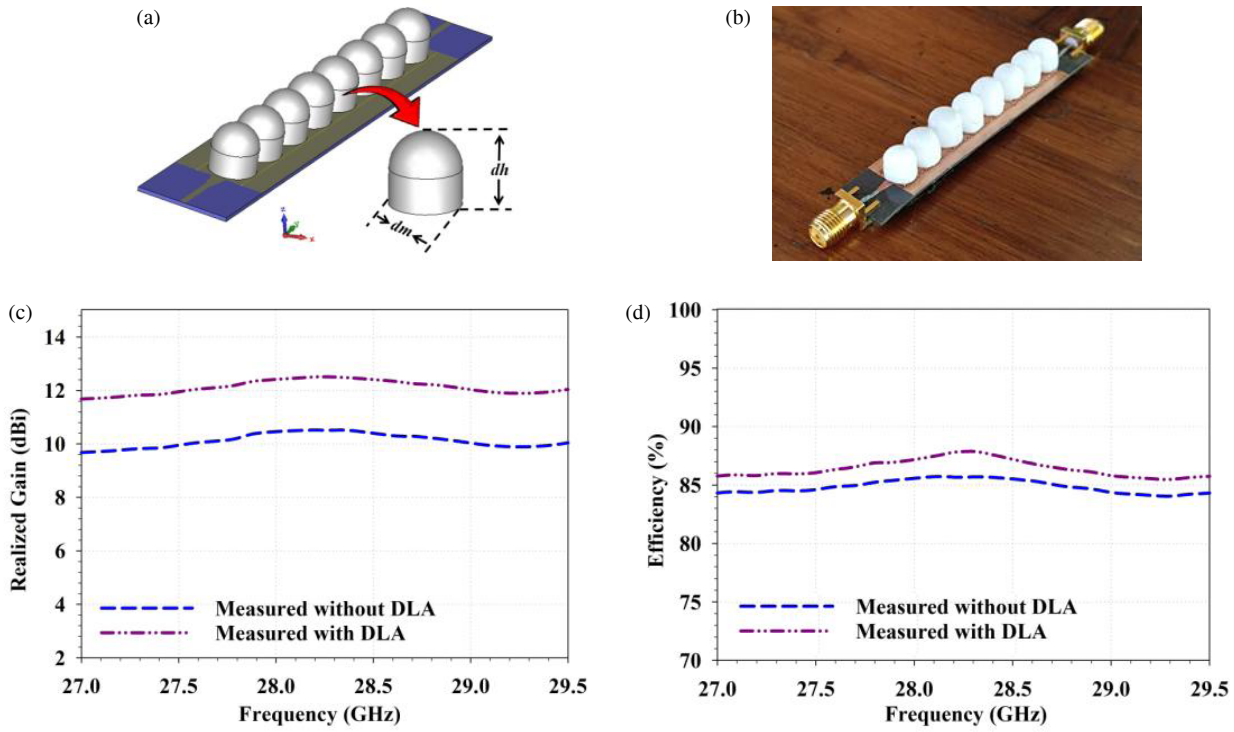

FIGURE 9. The DLA configuration, (a) simulated model, (b) fabricated prototype, (c) gain, and (d) radiation efficiency.

6. EXPERIMENTAL VALIDATION

The antenna was fabricated on an RT/Duroid 5880 substrate, as shown in Figure 10(a). The via section was drilled with a 0.3 mm-diameter drill bit, and a copper stitching method was employed for via placement. This approach eliminates solder residues and minimizes unintended physical alterations to the surface, thereby preserving the antenna's performance. Both ends of the antenna were interconnected using 35 GHz wide-bandwidth SMA connectors to ensure good signal integrity during measurements. The experimental validation was carried out using a Keysight-N5227B 67 GHz vector network analyzer as

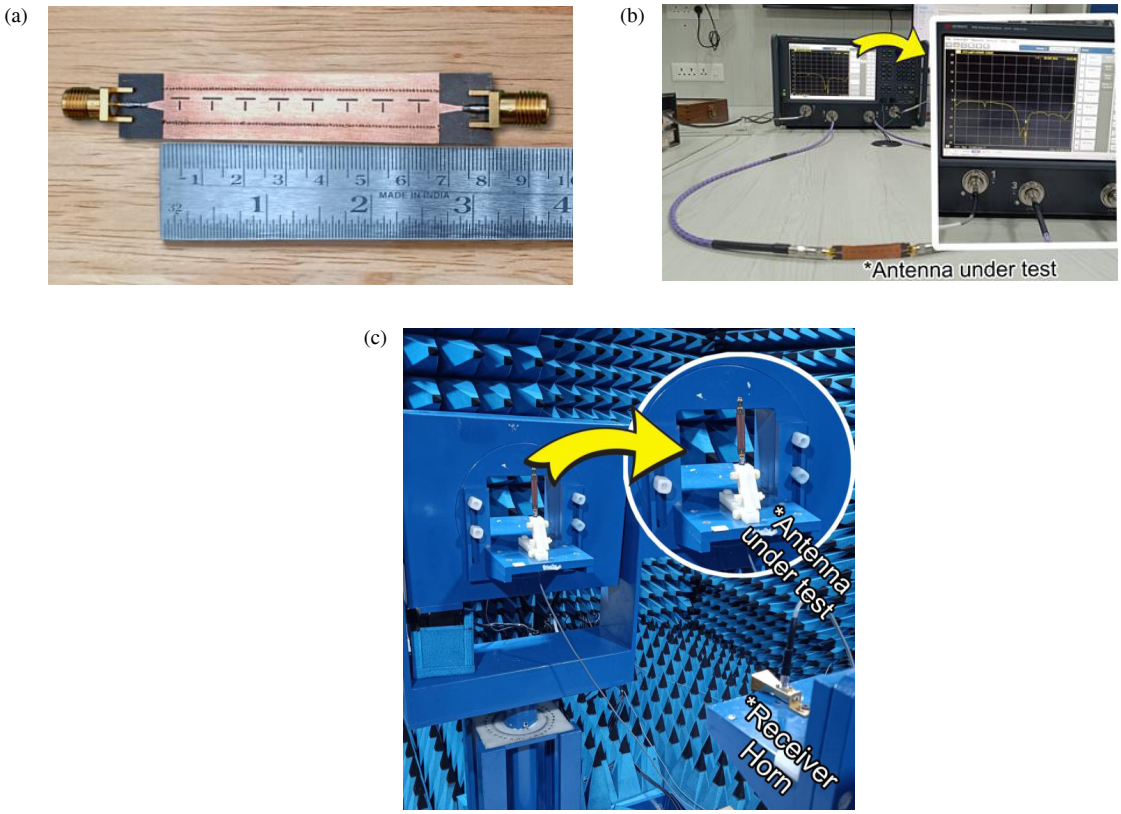

FIGURE 10. Antenna setup and measurement, (a) proposed antenna prototype, (b) measurement setup, and (c) anechoic chamber setup.

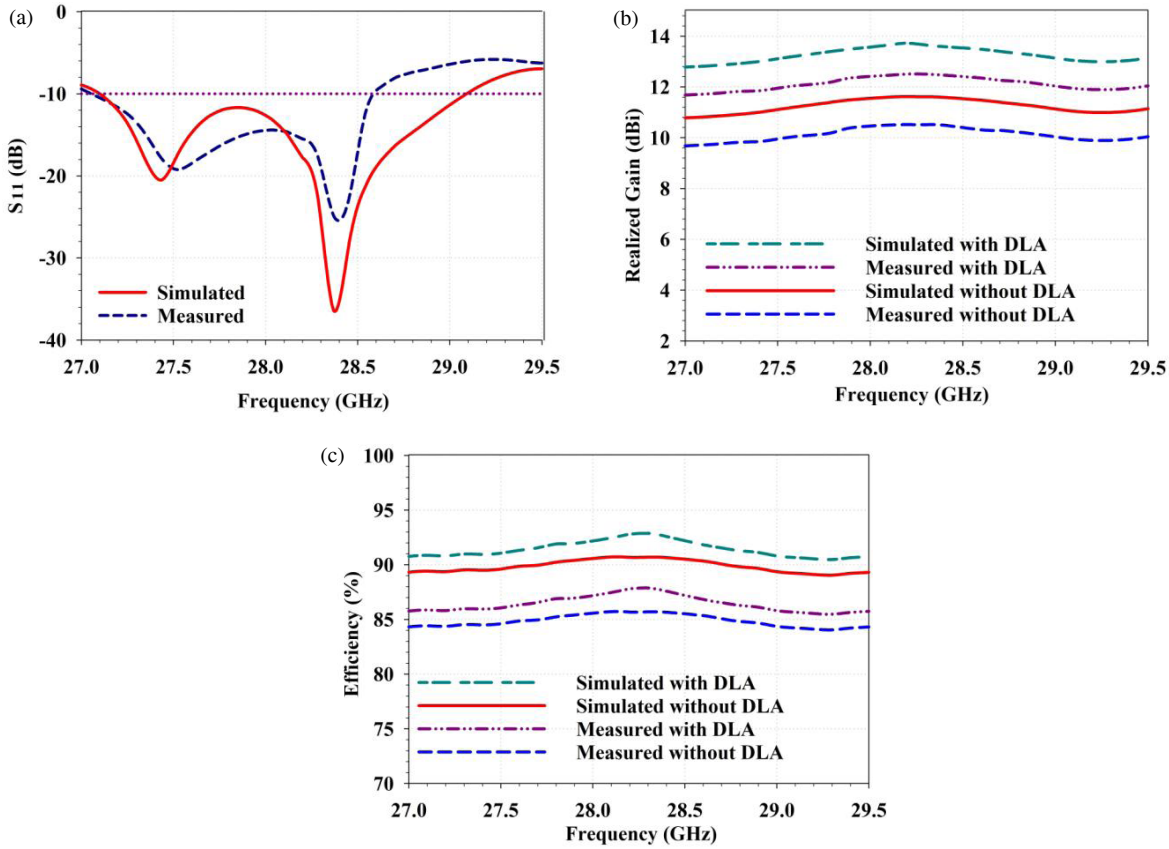

FIGURE 11. Experimental validation, (a) S_{11} parameters, (b) gain, and (c) radiation efficiency.

TABLE 2. Comparison of antenna performance matrices.

Ref	Antenna Structure	Operating Frequency (GHz)	HPBW (Degree)	XPD (dB)	Gain (dBi)	Gain Per Unit Cell (dBi)	Electrical Size (λ_o^3)	Radiation Efficiency (%)
[7]	λ-shaped SIW Antenna	10.76/12.39	Omni Directional	18.5	6.12/6.15	-	$1.027 \times 1.35 \times 0.025$	82.5
[8]	T-Shaped SIW Antenna	8.8–10.9	120	-	7.3	-	$0.63 \times 1.07 \times 0.03$	86
[9]	L-Shaped SIW Array Antenna	9.4–10.5	Omni Directional	23	9.5	7.8	$0.46 \times 2.1 \times 0.025$	-
[10]	1×4 SIW Dipole Array Antenna	24.12–30.83	60	-	11.02	6.98	$2.30 \times 4.38 \times 0.27$	-
[11]	CSRR-Based SIW Antenna	10.2/16.9	22	25	11.6/11.2	4.61/4.21	$3.15 \times 1.80 \times 0.028$	-
[12]	Cavity-backed Metamaterial SIW Antenna	27.42/28.70	54	-	6.40/4.77	5.72	$1.34 \times 0.93 \times 0.046$	-
[13]	SIW-Slot Array Antenna	28	16	30	13	3.97	$0.667 \times 4.84 \times 0.023$	-
[14]	Cavity-backed SIW Antenna	14.43-16.49	140	10	4.7	-	$0.77 \times 1.63 \times 0.07$	-
[15]	L-Shaped SIW Antenna	26–28	Omni Directional	35	7.5	-	$1.26 \times 1.62 \times 0.0708$	90
[16]	Mushroom Patch SIW Antenna	25.98–40.18	Omni Directional	38	7.2	-	$1.12 \times 1.21 \times 0.07$	85
This Work	**NIAT-SIW Antenna**	**27–28.54**	**8.1**	**25**	**10.51**	**2.20**	$\mathbf{6.30 \times 1.07 \times 0.046}$	**84.82**
	NIAT-SIW DLA	**27–28.54**	**8.1**	**25**	**12.50**	**4.65**	$\mathbf{6.30 \times 1.07 \times 0.046}$	**86.35**

shown in Figure 10(b). The radiation pattern measurements are conducted in an anechoic chamber, as shown in Figure 10(c). The simulated and measured reflection coefficients are presented in Figure 11(a). A bandwidth deviation of 360 MHz (1.22%) is observed between the simulated and measured results, especially in the upper-frequency region. This shift is mainly attributed to fabrication tolerances, SMA connector soldering losses, and slight variations in substrate parameters. The gain and efficiency matrices are shown in Figure 11(b) and Figure 11(c), respectively. The performance comparison presented in Table 2 highlights that the proposed antenna achieves higher gain, enhanced XPD levels, improved efficiency, and a highly focused narrow beam compared to existing designs reported in the literature.

7. CONCLUSION

A compact, high-gain millimeter-wave SIW antenna is presented for precision radar sensing and n-257 5G communication applications. The antenna operates over a bandwidth of 27 GHz to 28.54 GHz, covering the n-257 5G band spectrum with stable performance across the desired frequency range. The proposed design exhibits a highly directive radiation pattern with a narrow beamwidth of 8.1°, low side-lobe levels, and excellent XPD levels, making it suitable for high-resolution mm-Wave radar sensing. The antenna achieves a peak gain of 10.51 dBi with a radiation efficiency of 84.82%. With the adoption of a DLA configuration, the gain is enhanced to 12.50 dBi, with an improved radiation efficiency of 86.35%. Overall, the proposed antenna combines compact size, high gain, improved efficiency, and focused radiation beam characteristics, making it an ideal choice for next-generation mm-Wave radar systems and point-to-point 5G portable wireless communication applications.

ACKNOWLEDGEMENT

This work was carried out independently without any financial support from public, commercial, or non-profit organizations.

REFERENCES

[1] Redondi, A. E. C., C. Innamorati, S. Gallucci, S. Fiocchi, and F. Matera, "A survey on future millimeter-wave communication applications," *IEEE Access*, Vol. 12, 133 165–133 182, 2024.

[2] Kumar, S., A. S. Dixit, R. R. Malekar, H. D. Raut, and L. K. Shevada, "Fifth generation antennas: A comprehensive review of design and performance enhancement techniques," *IEEE Access*, Vol. 8, 163 568–163 593, 2020.

[3] Aggarwal, R., A. Roy, and R. Kumar, "Millimeter wave antennas: A state-of-the-art survey of recent developments, principles, and applications," *Progress In Electromagnetics Research B*, Vol. 104, 147–169, 2024.

[4] Ananthasankar, U. A., T. K. Rekha, and K. K. Ansha, "Ultra wide band circularly polarized slotted waveguide antenna for sub-terahertz wireless networks," *Next Research*, Vol. 2, No. 4, 100954, 2025.

[5] Aggarwal, R., A. Roy, and R. Kumar, "Millimeter wave antennas: A state-of-the-art survey of recent developments, principles, and applications," *Progress In Electromagnetics Research B*, Vol. 104, 147–169, 2024.

[6] Yang, Y., M. Mao, J. Xu, H. Liu, J. Wang, and K. Song, "Millimeter-wave antennas for 5G wireless communications: Technologies, challenges, and future trends," *Sensors*, Vol. 25, No. 17, 5424, 2025.

[7] Asaithambi, R., M. P. Prabakaran, and G. Rajesh, "A self-diplexing multi-mode SIW cavity-backed antenna with a lambda(λ)-shaped slot for X- and Ku-band applications," *Progress In Electromagnetics Research C*, Vol. 165, 257–266, 2026.

[8] Wu, Q., J. Yin, C. Yu, H. Wang, and W. Hong, "Broadband planar SIW cavity-backed slot antennas aided by unbalanced shorting vias," *IEEE Antennas and Wireless Propagation Letters*, Vol. 18, No. 2, 363–367, Feb. 2019.

[9] El khamlichi, D., N. A. Touhami, T. Elhamadi, and M. A. Ennasar, "High-gain and broadband SIW cavity-backed slots antenna for X-band applications," *International Journal of Microwave and Wireless Technologies*, Vol. 13, No. 10, 1078–1085, 2021.

[10] Gao, M., R. Huang, X. Du, and B. Tao, "Design of a three-layer SIW broadband 1 × 4 dipole patch array antenna driven by slot feeding," *Progress In Electromagnetics Research C*, Vol. 168, 138–148, 2026.

[11] Maruti, A. M. and B. S. N. Kishore, "Dual-band SIW slot array filtering antenna for X and Ku band applications," *Progress In Electromagnetics Research Letters*, Vol. 103, 109–117, 2022.

[12] Sharma, A. and R. Budhiraja, "A slot array cavity backed SIW metamaterial antenna for satellite applications," *Progress In Electromagnetics Research B*, Vol. 109, 113–125, 2024.

[13] Bharath, K., S. V. Nandigama, D. Ramakrishna, and V. M. Pandharipande, "High performance millimeter wave SIW slotted array antenna," *Progress In Electromagnetics Research C*, Vol. 125, 15–23, 2022.

[14] Kumar, A. and S. Raghavan, "Broadband SIW cavity-backed triangular-ring-slotted antenna for Ku-band applications," *AEU — International Journal of Electronics and Communications*, Vol. 87, 60–64, 2018.

[15] Kumar, L., V. Nath, and B. Reddy, "A wideband substrate integrated waveguide (SIW) antenna using shorted vias for 5G communications," *AEU — International Journal of Electronics and Communications*, Vol. 171, 154879, 2023.

[16] El-Arrouch, T., A. E. Ansari, N. E. A. E. Idrissi, M. Trimukhe, S. K. Khandare, Z. Zakaria, and A. J. A. Al-Gburi, "A compact parasitic mushroom patch loaded antenna for 5G mm-Wave applications (28 GHz /38 GHz)," *Progress In Electromagnetics Research B*, Vol. 113, 13–22, 2025.

[17] Kho, E., B. Basu, and A. Nandi, "High-gain, low-SLL SIW filtenna with enhanced frequency selectivity for Ku-band wireless systems," *AEU — International Journal of Electronics and Communications*, Vol. 200, 155850, 2025.

[18] Mashayekhi, M., K. Salehian, A. Ozgoli, S. Abdollahi, A. Abdipour, and A. A. Kishk, "AI-powered inverse design of Ku-band SIW resonant structures by iterative residual correction network," *AEU — International Journal of Electronics and Communications*, Vol. 201, 156003, 2025.

[19] Hosseininejad, S. E., N. Komjani, and A. Mohammadi, "Accurate design of planar slotted SIW array antennas," *IEEE Antennas and Wireless Propagation Letters*, Vol. 14, 261–264, 2015.

[20] Saxena, S., N. Tewari, and S. Srivastava, "A spiral cavity-backed 4 × 4 MIMO SIW antenna at Ku-band for radio telescopes," *Progress In Electromagnetics Research M*, Vol. 132, 1–10, 2025.

[21] Wang, Y.-S. and S.-J. Chung, "A short open-end slot antenna with equivalent circuit analysis," *IEEE Transactions on Antennas and Propagation*, Vol. 58, No. 5, 1771–1775, May 2010.

[22] Deslandes, D., "Design equations for tapered microstrip-to-substrate integrated waveguide transitions," in *2010 IEEE MTT-S International Microwave Symposium*, 704–707, Anaheim, CA, USA, 2010.

[23] Huang, T.-Y., T.-M. Shen, and R.-B. Wu, *Design and Modeling of Microstrip Line to Substrate Integrated Waveguide Transitions*, Passive Microwave Components and Antennas. InTech, 2010.